iScience

CellPress

Article

A "σ-Hole"-Containing Volatile Solid Additive Enabling 16.5% Efficiency Organic Solar Cells

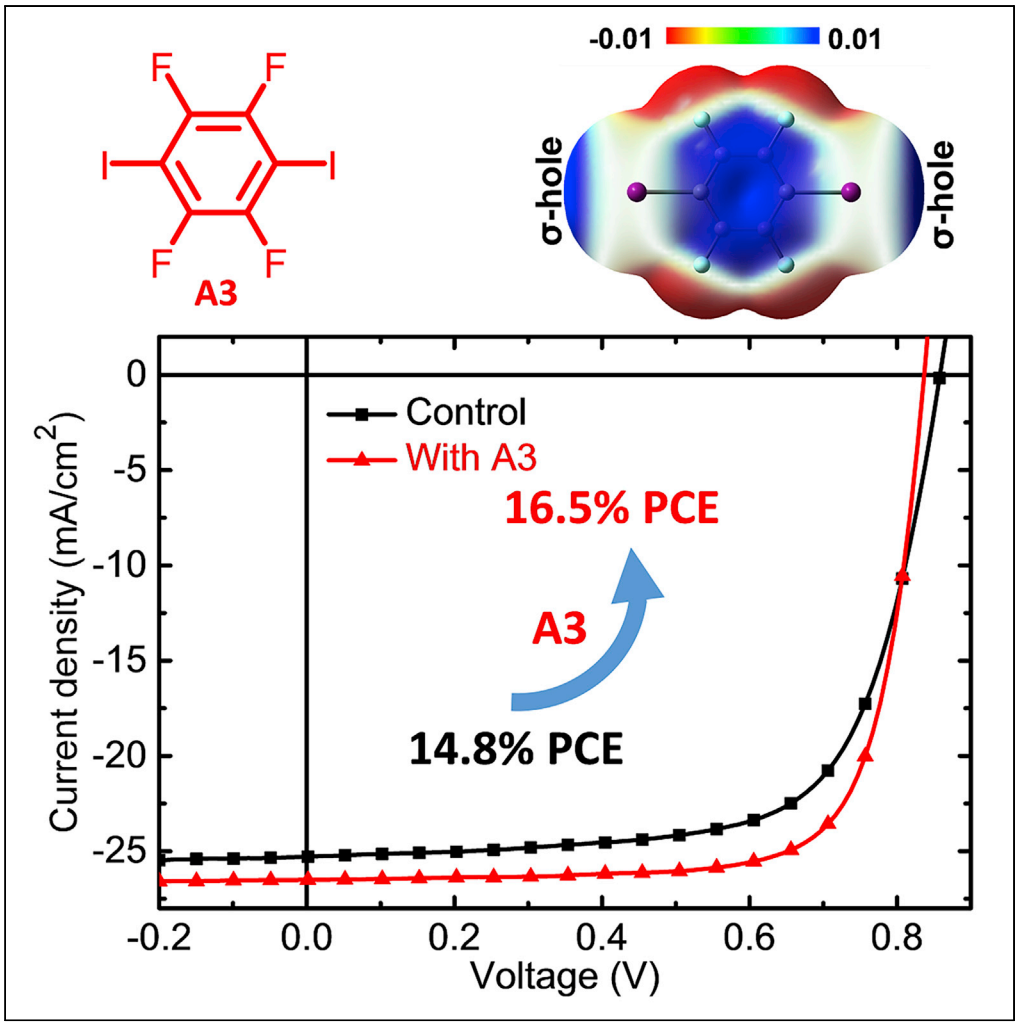

Jiehao Fu, Shanshan Chen, Ke Yang, ..., Shirong Lu, Zeyun Xiao, Yongfang Li

kuan.sun@cqu.edu.cn (K.S.)
lushirong@cigit.ac.cn (S.L.)
xiao.z@cigit.ac.cn (Z.X.)

HIGHLIGHTS

A "σ-hole"-containing small molecule is used as an additive for organic solar cells

16.5% efficiency organic solar cells are achieved with additive engineering

Excellent stability and easy processability are obtained with the additive

Fu et al., iScience *23*, 100965
March 27, 2020
https://doi.org/10.1016/j.isci.2020.100965

iScience

CellPress

Article

A ''σ-Hole''-Containing Volatile Solid Additive Enabling 16.5% Efficiency Organic Solar Cells

Jiehao Fu,[1,2,5] Shanshan Chen,[2,5] Ke Yang,[1,2] Sungwoo Jung,[3] Jie Lv,[1] Linkai Lan,[1,2] Haiyan Chen,[1] Dingqin Hu,[1] Qianguang Yang,[1] Tainan Duan,[1] Zhipeng Kan,[1] Changduk Yang,[3] Kuan Sun,[2,*] Shirong Lu,[1,*] Zeyun Xiao,[1,6,*] and Yongfang Li[4]

SUMMARY

Here we introduce a σ-hole-containing volatile solid additive, 1, 4-diiodotetrafluorobenzene (A3), in PM6:Y6-based OSCs. Aside from the appropriate volatility of A3 additive, the synergetic halogen interactions between A3 and photoactive matrix contribute to more condensed and ordered molecular arrangement in the favorable interpenetrating donor/acceptor domains. As a result, greatly accelerated charge transport process with suppressed charge recombination possibility is observed and ultimately a champion PCE value of 16.5% is achieved. Notably, the A3 treated OSCs can maintain a high efficiency of over 16.0% in a wide concentration range of A3 additive between 10 and 35 mg/mL. The A3-treated device shows excellent stability with an efficiency of 15.9% after 360-h storage. This work demonstrates that the σ-hole interaction can be applied to enhance the OSC performance and highlights the importance of non-covalent interactions in the optoelectronic materials.

INTRODUCTION

Recent progress in organic solar cells (OSCs), especially the advents of non-fullerene acceptors like ITIC and Y6 (Yuan et al., 2019; Lin et al., 2015), shows a bright future for organic photovoltaic industry. It is well known that the morphology of active layer plays a vital role in OSC's performance. To ensure an appropriate donor/acceptor (D/A) bulk heterojunction (BHJ) morphology for exciton dissociation, charge carrier generation, and transport, a variety of methods like thermal annealing (TA), (Kim et al., 2005; Li et al., 2005; Erb et al., 2005; Ma et al., 2010), solvent vapor annealing (SVA), and additive engineering are employed (Sun et al., 2014, 2015; Li et al., 2010; Peet et al., 2006, 2007; Rogers et al., 2011; Lee et al., 2008; Hoven et al., 2010). Among the approaches above, the additive engineering has been identified as the most effective way to control the nanostructure of interpenetrating donor/acceptor domains in BHJ for efficient charge carrier separation and transport. Currently, a large number of high-performance OSCs are assisted by additives (Yuan et al., 2019; Cui et al., 2019; Hong et al., 2019; Yan et al., 2019; Zhang et al., 2018a; Li et al., 2018; Zhao et al., 2017; Baran et al., 2016; Fei et al., 2018; Jiang et al., 2019; Pan et al., 2019; Yu et al., 2019). Traditional solvent additives like 1, 8-diiodooctane (DIO) and 1-chloronaphthalene (CN) are able to modulate the distribution of donor and acceptor components during film deposition process and thus improve device performance (Mcdowell et al., 2018). However, the volume of solvent additives needs to be controlled carefully in a low concentration, which is generally less than 3% or even 0.5% (v/v) (Baran et al., 2016; Cui et al., 2019; Hong et al., 2019; Yan et al., 2019; Zhang et al., 2018a; Zhao et al., 2017; Jiang et al., 2019; Pan et al., 2019). The variation of additive amount can make a huge difference to device performance, leading to poor reproducibility of OSCs. Besides, the traditional high-boiling-point solvent additives normally generate devices with poor stability, which could be attributed to the residue of additive deteriorating the BHJ morphology (Yu et al., 2018; Villers et al., 2016; Tournebize et al., 2015). Furthermore, in terms of the fundamental mechanism, CN and DIO additives are initially designed for fullerene-based OSC systems owing to their low volatility and selective solubility of one components (Lee et al., 2008; Machui et al., 2015; Manley et al., 2017), whereas in the non-fullerene OSCs, the skeletons of acceptors are mainly based on planar conjugated backbones and abundant group IV–VII elements (e.g., N, S) are presented. These features are different from that of the fullerene acceptors like $PC_{60}BM$ and $PC_{70}BM$ (Yuan et al., 2019; Lin et al., 2015; Hummelen et al., 1995; Wienk et al., 2003). It is of great importance to explore new types of additives that are more compatible with non-fullerene OSC systems.

[1]Organic Semiconductor Research Center, Chongqing Institute of Green and Intelligent Technology, Chongqing School, University of Chinese Academy of Sciences (UCAS Chongqing), Chinese Academy of Sciences, Chongqing 400714, P. R. China

[2]Key Laboratory of Low-grade Energy Utilization Technologies and Systems, CQU-NUS Renewable Energy Materials & Devices Joint Laboratory, School of Energy & Power Engineering, Chongqing University, Chongqing 400044, P. R. China

[3]Department of Energy Engineering, School of Energy and Chemical Engineering, Perovtronics Research Center, Low Dimensional Carbon Materials Center, Ulsan National Institute of Science and Technology (UNIST), 50 UNIST-gil, Ulju-gun, Ulsan 44919, Republic of Korea

[4]Beijing National Laboratory of Molecular Sciences, CAS Key Laboratory of Organic Solids, Institute of Chemistry, Chinese Academy of Sciences, Beijing 100190, P. R. China

[5]These authors contributed equally

[6]Lead Contact

*Correspondence: kuan.sun@cqu.edu.cn (K.S.), lushirong@cigit.ac.cn (S.L.), xiao.z@cigit.ac.cn (Z.X.)

https://doi.org/10.1016/j.isci.2020.100965

The "σ-hole" refers to the electron-deficient region on a group IV–VII atom when it covalently bonded to electron-withdrawing groups. It has been widely accepted that the σ-hole can form non-covalent interaction with lone electron pairs (e.g., the lone electron pair of N and S), namely, σ-hole interaction. This non-covalent intermolecular interaction has been found tremendous applications in supramolecular recognition and regulating self-assembly nanostructures (Lim and Beer, 2018; Cavallo et al., 2016; Kolář and Hobza, 2016). It should be noted that the phase separation process of donor/acceptor materials is also a self-assembly process. Even though abundant lone electron pairs are presented in the donor and acceptor materials, which provide binding sites for the σ-hole interaction, this non-covalent interaction has been scarcely discussed in organic solar cells.

In this work, we employed a σ-hole-containing additive to modulate donor/acceptor phase separation. Taking into account that the introduction of σ-hole-containing additive could also be an "impurity," a volatile one (1, 4-diiodotetrafluorobenzene, A3) was chosen in this strategy. A3 has been frequently used as halogen bond donor in crystal engineering (Cavallo et al., 2016). Owing to the synergetic halogen bonding interaction between additive and photoactive materials, the volatilization of A3 from the photoactive layer induces the BHJ nanostructure rearrangement, giving larger crystalline sizes, denser molecule stacking, and thus better charge transport property in devices. The PCE values of OSCs based on polymer donor (PM6) and small molecular acceptor (Y6) system dramatically increased from 14.8% to 16.5% (certified as 15.9%) by using A3 volatile additive, much higher than the reported one (certified as 14.9%) using the 1-chloronaphthalene (CN) solvent additive (Yuan et al., 2019). Even when the concentration of the additive in precursor solution increased up to 50 mg/mL, nearly 600 wt% of the acceptor component in blend, A3 additive processing still provides a PCE of 15.7%, which greatly contributes to the easy processability.

RESULTS

The Promotion of Device Performance through Introducing A3

Figure 1 shows the chemical structures of polymer donor (PM6), non-fullerene small molecular acceptor (Y6), and volatile solid additive (A3) used in this work. The OSCs were fabricated with a conventional device structure of indium tin oxide (ITO)/poly (3,4-ethylenedioxythiophene):poly (styrenesulfonate) (PEDOT:PSS)/photoactive layer/(2-(1,10-phenanthrolin-3-yl) naphth-6-yl) diphenylphosphineoxide (Phen-NaDPO)/Ag (Tan et al., 2015). Besides, density functional theory (DFT) simulation (Figure 1E) shows that A3 possesses σ-holes, which can be used to study the σ-hole interaction in OSCs. As shown in Table S1, the highest power conversion efficiency (PCE) value of 14.8% was obtained in the control devices with an open-circuit voltage (V_{OC}) of 0.86 V, a short circuit current density (J_{SC}) of 25.3 mA/cm^2, and a fill factor (FF) of 68.4%. Upon introducing A3 volatile additive into the blend, the PCE of OSC was enhanced to 15.2% at an optimized concentration of 15 mg/mL. TA process at 110°C for 10 min was additionally conducted to help remove the residue of A3 in blend film. As a result, a champion PCE value of 16.5% with a slightly deceased V_{oc} (0.82 V) but significantly enhanced J_{SC} (26.5 mA/cm^2) and FF (76.1%) parameters was achieved (Table 1). Besides, the PCEs of the A3-treated devices can maintain over 16.0% in a broad additive concentration ranging from 10 to 35 mg/mL in the precursor solution. It is worth mentioning that, even when the concentration of A3 raised to 50 mg/mL, three times higher than the total concentration of PM6 and Y6 in blend, a favorable efficiency of 15.7% was retained, higher than the control counterpart. The typical current density-voltage (J–V) characteristics of the optimized devices and corresponding external quantum efficiency (EQE) spectra are presented in Figures 1F and 1I. Compared with the control device, A3-treated counterpart shows a slight shift in EQE spectra. This shift is partially related to the absorption of acceptor as a similar absorption shift induced by A3 additive can be observed for Y6+A3 film (Figure 4D). The integrated J_{SC} values of the control and the A3-treated device from the EQE spectra are 24.5 and 25.7 mA/cm^2, respectively, which are consistent with the results acquired from the *J–V* measurements. In addition, a certificated PCE of 15.9% was obtained from the National Institute of Metrology (NIM) in Beijing, China (Figure S9). The improvement on the device performance was attributed to the A3 additive, which enhances carrier mobility in the active layer and provides more balanced charge transport property. Meanwhile, the A3 treated devices show longer carrier lifetime, shorter charge extraction time, and suppressed recombination as evidenced by device physics studies. Thus, distinctly enhanced PCE value of 16.5% in binary single-junction OSCs is achieved. To verify the versatility of A3, we also introduced this additive in OSCs based on PBDB-T: Y6 and PBDB-T-SF: IT-4F (Figure S1). A3 additive treatment contributed to higher J_{SC} and FF in both two OSC systems (Table S2), which is consistent with the trend observed in the PM6: Y6-based OSCs.

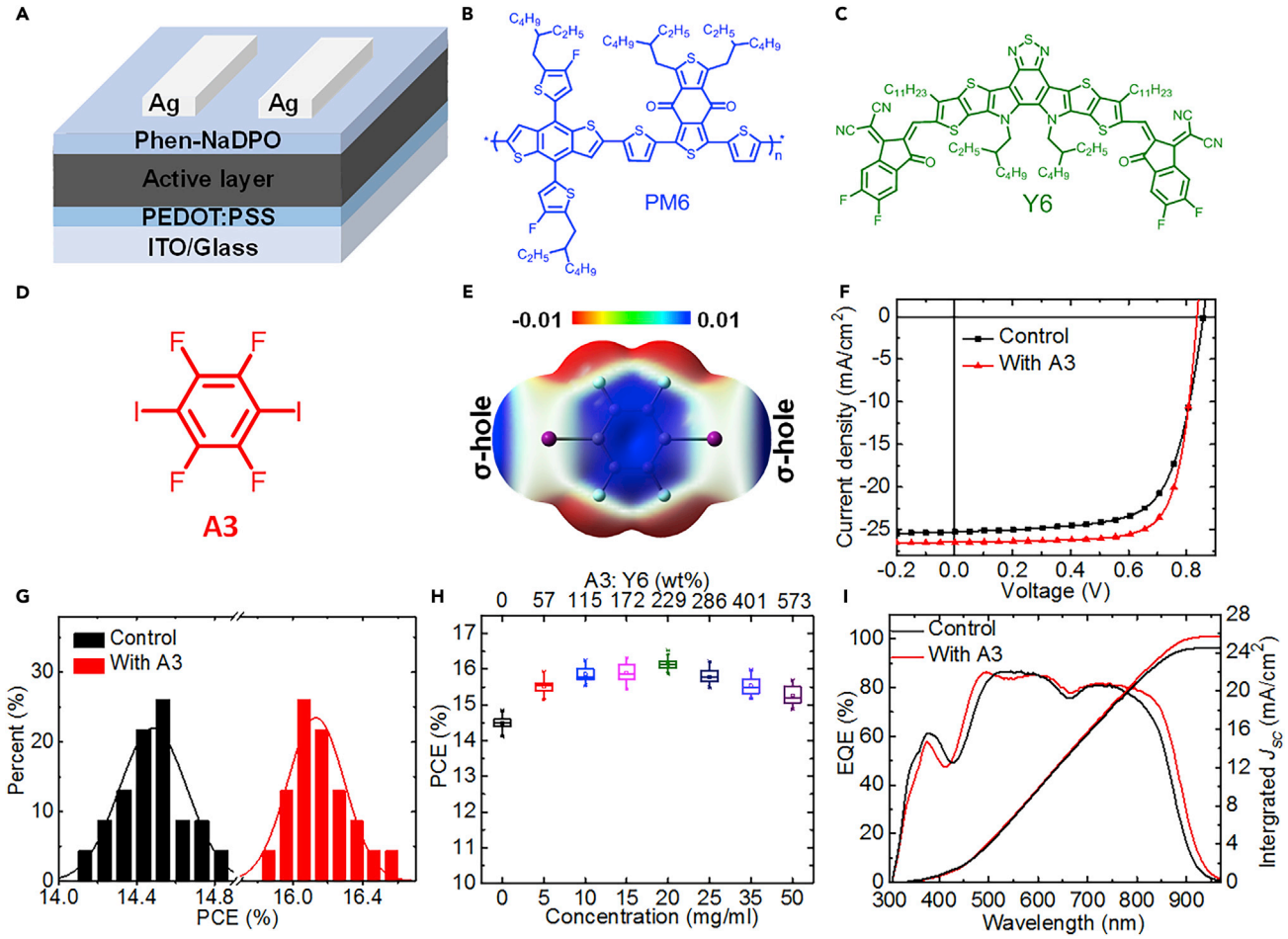

Figure 1. Device Structure, Molecule Structures, and Photovoltaic Performances

(A) Schematic illustration of the device structure employed in this work.

(B) Molecular structure of the polymer donor PM6.

(C) Molecular structure of the acceptor Y6.

(D) Molecular structure of the additive A3.

(E) The theoretically simulated electrostatic potential distribution (ESP) of A3 calculated from the density functional theory (DFT) at the BLYP/6–31G level. The colors changing from red to blue indicate the increasing ESP from negative to positive.

(F) J–V curves of PM6: Y6-based OSCs with/without A3 tested in the air under 1,000 W/m2 AM 1.5G illumination.

(G) PCE histograms PM6: Y6-based OSCs with/without A3 tested in the air under 1,000 W/m2 AM 1.5G illumination.

(H) PCEs of A3-assisted PM6:Y6 devices as a function of the weight ratios of A3:Y6.

(I) EQE curves and the corresponding integrated J_{SC} values of PM6:Y6-based devices with/without A3 additive.

The Charge Transport, Recombination, and Extraction Properties of Devices with or without A3

To investigate the effects of A3 treatment on the charge transport, recombination, and extraction properties in OSCs, the space charge limited current (SCLC) method was used to probe the charge carrier mobilities of both the control and A3-treated blend film. The current-voltage ($J^{1/2}$–V) characteristics are presented in Figures 2A and 2B, and the corresponding mobility data are listed in Table S3. For the control blend, the mobilities of hole and electron are 3.08×10^{-4} and 1.32×10^{-4} cm^2/Vs, respectively. For the A3-processed blend, both parameters climb to 4.84×10^{-4} and 3.96×10^{-4} cm^2/Vs, respectively. The enhanced carrier mobility and more balanced charge transport property should contribute to the reduction of space current and thereby better device performance.

Transient photovoltage (TPV) and transient photocurrent (TPC) measurements were carried out to evaluate the charge extraction time and carrier lifetime in OSCs. As shown in Figure 2C, the charge carrier lifetime of

Concentration of Additive (mg/mL)	V_{OC} (V)	J_{SC} (mA cm^{-2})	FF (%)	PCE[a] (%)
0 (Control)[b]	0.86	25.29	68.40	14.8 (14.4 ± 0.2)
CN-0.05 v%[c]	0.84	25.46	72.90	15.6 (15.3 ± 0.2)
A3-5 mg/mL[c]	0.84	25.66	73.90	15.9 (15.5 ± 0.2)
A3-10 mg/mL[c]	0.84	26.04	74.27	16.2 (15.9 ± 0.2)
A3-15 mg/mL[c]	0.83	26.26	74.82	16.3 (15.9 ± 0.2)
A3-20 mg/mL[c]	0.82	26.50	76.05	16.5 (16.1 ± 0.2)
A3-25 mg/mL[c]	0.82	26.28	75.21	16.2 (15.8 ± 0.2)
A3-35 mg/mL[c]	0.81	26.08	75.64	16.0 (15.5 ± 0.2)
A3-50 mg/mL[c]	0.81	25.79	75.11	15.7 (15.3 ± 0.3)

Table 1. Photovoltaic Performances of PM6:Y6-Based OSCs with Different Concentration of A3 Additive

[a]The highest and average PCEs with standard deviation calculated from 20 devices.

[b]Devices without any treatment and tested in the air without encapsulation.

[c]Devices with TA treatment and tested in the air without encapsulation.

the solar cells processed with volatile A3 additive is 25.2 μs, which is much longer than that of the control one (18.5 μs). Furthermore, the TPC results (Figure 2D) show that the charge extraction time decreases from 0.36 μs (the control one) to 0.26 μs (A3-processed one). In general, longer carrier lifetime and shorter charge extraction time suggest slower recombination rates. Therefore, the results above suggest that the charge recombination was greatly suppressed via utilizing the volatile A3 additive in blend (Liang et al., 2018). The σ-hole interactions between A3 and photoactive matrix contribute to the more condensed and ordered molecular arrangement in the favorable interpenetrating donor/acceptor domains. This is supported by the morphology studies including atomic force microscopy (AFM) and GIWAXS measurements. As a result, greatly accelerated charge transport process with suppressed charge recombination possibility is observed.

Morphology and Crystalline Ordering of Active Layer with or without A3

To explore the nanostructures in the photoactive layer and its correlation with the photovoltaic properties of the respect devices, tapping-mode AFM was initially performed to probe the surface morphology of the blend films. As shown in Figure 3, the AFM height images of both blend films show similar smooth surface with low root-mean-square roughness (R_q) of 0.96–1.00 nm (Figures 3A and 3D), whereas the corresponding phase images clearly reveal that the A3-processing technique can adjust the nanoscale texture of the blend as evidenced by larger feature size induced by A3. As shown in Figures 3B and 3E, the control blend film exhibited phase-separated regions with a defined fibril-like feature, whereas densely interconnected networks are observed in the A3-treated blend film, indicating that the A3 additives assisted the self-assembly process and regulate the microstructure morphology formation. The morphology changes are related to the σ-hole interaction between A3 and aromatic fragments containing S or N atoms, which was proved by Fourier transform infrared (FTIR) spectroscopy, UV-vis, and ^{19}F NMR. It should be noted that, the morphology of A3 assisted PM6:Y6 film changes during annealing. The final film morphology with A3 treatment is different from a control film without A3 that undergoes the same annealing.

Grazing incidence wide-angle X-ray scattering (GIWAXS) measurement was conducted to further identify the crystalline ordering difference between the control and A3-treated blend films (Figures 3C and 3F). Both the control and A3-treated blend film show predominantly face-on orientation as revealed by the azimuthal pole figure (Figure S3D). The face-on orientation is thought to be favorable for device performance (Zhang et al., 2018b; Huang et al., 2018; Yang et al., 2015). For the face-on (010) diffractions, the π-stacking crystallite coherence length (CCL_{010}) values (Table S4), estimated from the Scherrer equation, are 26.75 and 27.63 Å for the control (q_z = 1.69 Å^{-1}) and A3-treated (q_z = 1.70 Å^{-1}) blend films, respectively, indicating the relatively larger (010) ordered crystallites and more compact molecular packing contained in the A3-treated system. The results demonstrate that the A3-treatment in PM6:Y6 blend matrix significantly

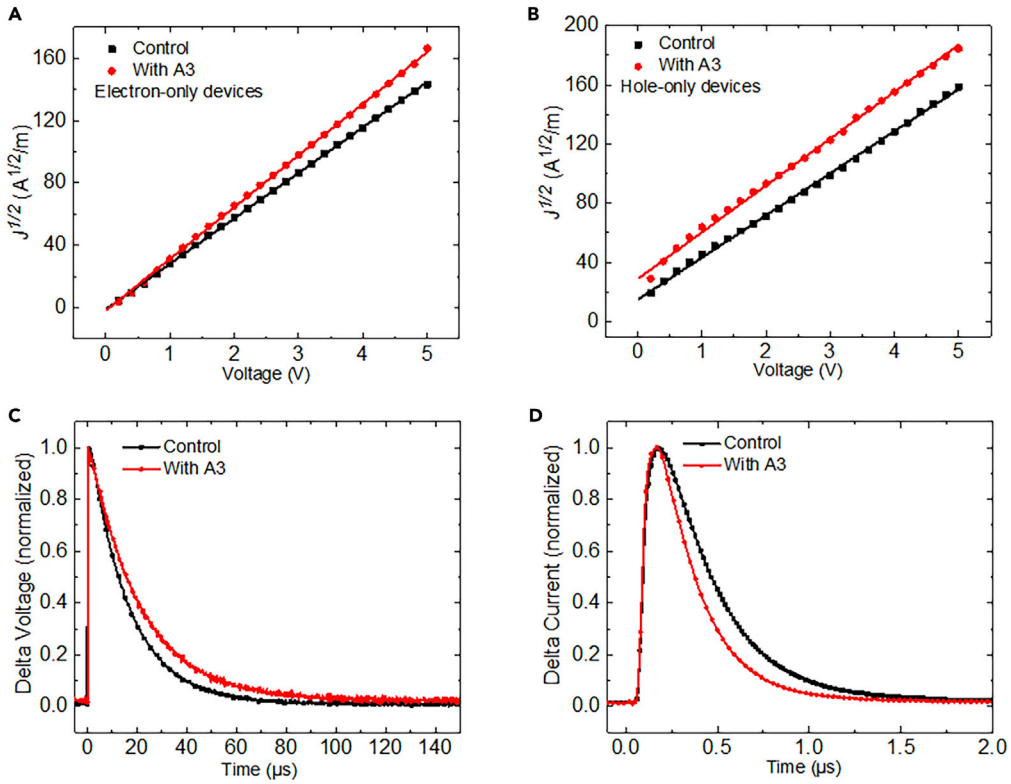

Figure 2. Charge Carrier Transport Properties

(A) The dark $J^{1/2}$-V curves of electron-only PM6:Y6 devices with and without A3 additive; see also Table S3.

(B) The dark $J^{1/2}$-V curves of hole-only PM6:Y6 devices with and without A3 additive; see also Table S3.

(C) TPV measurements for PM6:Y6 OSCs with and without A3 additive.

(D) TPC measurements for PM6:Y6 OSCs with and without A3 additive.

affects the molecular stacking distances and nanocrystalline size and maintains the molecular packing orientation. Considering the morphological properties mentioned before, one can speculate that the thermodynamically denser and enhanced π-π stacking feature with suitable phase-separated networks in blend is responsible for the simultaneously efficient charge transport and extraction processes, contributing to the higher power outputs in the A3-treated OSCs.

The Molecular Interaction between A3 and Active Materials

To further gain insight into the role of A3 additive in modulating the microstructure of solid state, UV-vis measurements were performed in the neat and blend films with/without A3-processing. The neat polymer donor PM6 film exhibits a broad absorption with maximum absorption at 616 nm. Upon introducing A3 additive at the same concentration of optimum devices, a strong vibronic shoulder is apparent at 578 and 622 nm (Figure 4A), probably attributed to the enhanced aggregation and ordered alignment of PM6 (Schulz and Ludwigs, 2017). Meanwhile, the introduction of A3 makes the maximum absorption peak of small molecular acceptor Y6 film shift from 818 to 826 nm (Figure 4D). The absorption of Y6 red shifted after the additive treatment, which could be attributed to the enhanced aggregation and ordered alignment of the molecules (Más-Montoya and Janssen, 2017). In addition, FTIR spectroscopy measurement was carried out to analyze the vibration frequency. As shown in Figures 4B and 4E, the peaks at 1456 and 563 cm^{-1} are assigned to the C-C and C-I stretching in neat A3 (Wang and Jin, 2017; Hanson et al., 2009), respectively. Compared with the neat A3, PM6:A3 and Y6:A3 blends exhibit obvious peak shifts, from 1456 to 1461 and 1463 cm^{-1}, respectively. Likewise, a secondary peak-shift phenomenon from 563 to 566 cm^{-1} is observed in both PM6:A3 and Y6:A3 blends. ^{19}F NMR studies of A3 upon addition of PM6 or Y6 reveals down field shift of the ^{19}F chemical shift further confirming the interaction of C-I bond and PM6 or Y6 molecules which in turn affect the chemical shift of F atoms (Figures 4C and 4F) (Sarwar et al.,

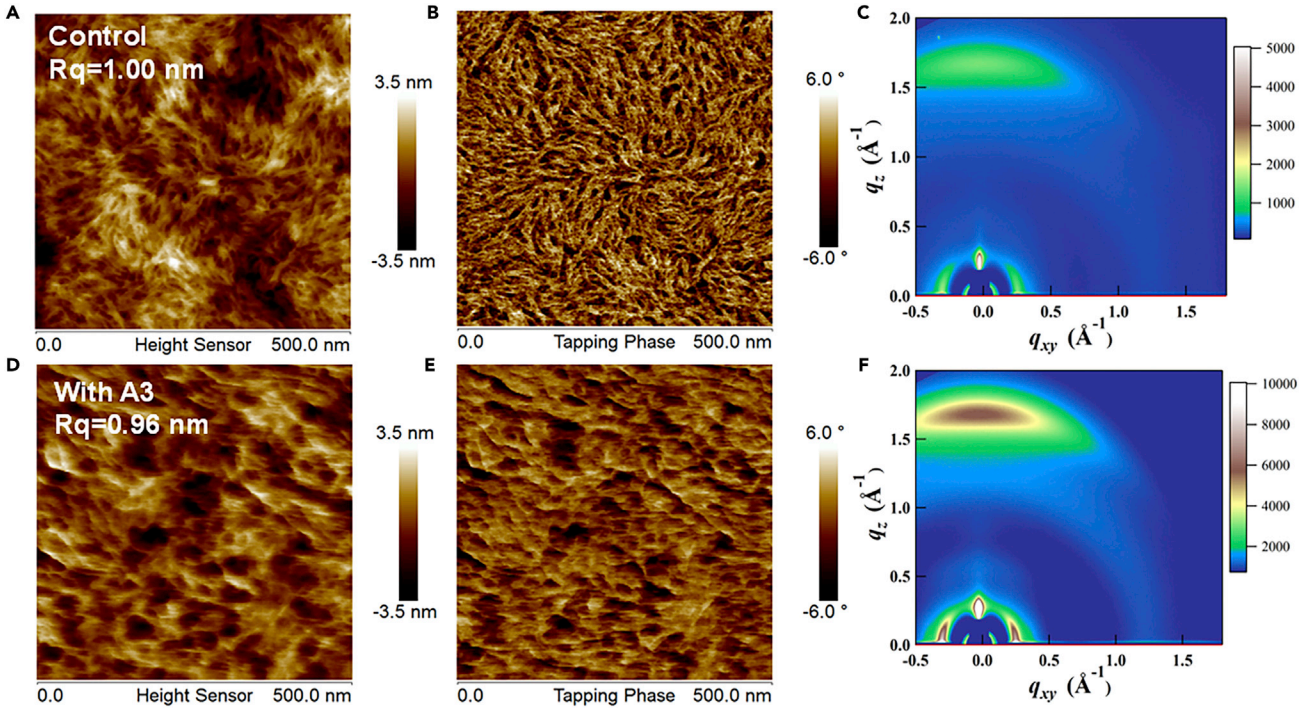

Figure 3. The Impact of A3 Additive on Blend Film Morphology and Crystallinity

(A) AFM height images of PM6:Y6 blend films without A3 additive.

(B) AFM phase images of PM6:Y6 blend films without A3 additive.

(C) GIWAXS two-dimensional diffraction patterns of PM6:Y6 blend films without A3 additive; see also Figure S3 and Table S4.

(D) AFM height images of PM6:Y6 blend films with A3 additive.

(E) AFM phase images of PM6:Y6 blend films with A3 additive.

(F) GIWAXS two-dimensional diffraction patterns of PM6:Y6 blend films with A3 additive; see also Figure S3 and Table S4.

Note: these blend films are fabricated following the process of device fabrication.

2010; Hanson et al., 2009). Such variational characteristics suggest that A3 simultaneously interacted with donor and acceptor components to fine-tune the BHJ morphology in blend.

We also studied the single component film morphology changes induced by A3 additive. As revealed by AFM studies, PM6 or Y6 film shows distinctively enhanced aggregation morphology after the A3 treatment further confirming the interaction (Figure S7). It is well known that A3 can interact with aromatic fragments containing S or N atoms through the formation of halogen bonding like C-I … π, C-I … S, and C-I … N (Hai et al., 2012; Wang and Jin, 2017; Liu et al., 2019a, 2019b). Thus, the halogen interactions between A3 and photoactive matrix might be the intrinsic driving force for the condensed molecular stacking behavior in blend. To validate the speculation, A3 analogs with different polarizability of halogens, hexafluorobenzene (A1) and 1, 4-dibromotetrafluorobenzene (A2) (Figure S8), were also examined in the PM6:Y6 system. In contrast to A1, both A2 and A3 can provide σ-hole due to the polarizability of electron clouds of Br/I. As a result, the A2-treated device provided an enhanced PCE of 16.1%, whereas the A1-treated device gave only an inferior PCE of 14.9% (Table S7).

The Superior Stability of Devices Treated by A3

Since the residue of volatile solid additive in the blend can act as a trap or barrier for charge transport, thorough evaporation of the A3 additive is necessary (Shockley and Jr, 1952). The volatility of A3 was in-deep characterized via thermogravimetric (TGA), UV-vis, and FTIR measurements. As shown in Figure S4A, when the heating rate was set as 1°C and 10°C min^{-1}, respectively, the corresponding evaporation temperatures (5% weight loss) of A3 are 88°C and 118°C, indicating the TA treatment at 110°C for 10 min is adequate for the removal of A3 in this work. The comparison of neat A3 absorption spectra before and after TA treatment confirms the complete volatilization of A3 (Figure S4B). Moreover, FTIR peaks at 1465, 939, and 566 cm^{-1} in

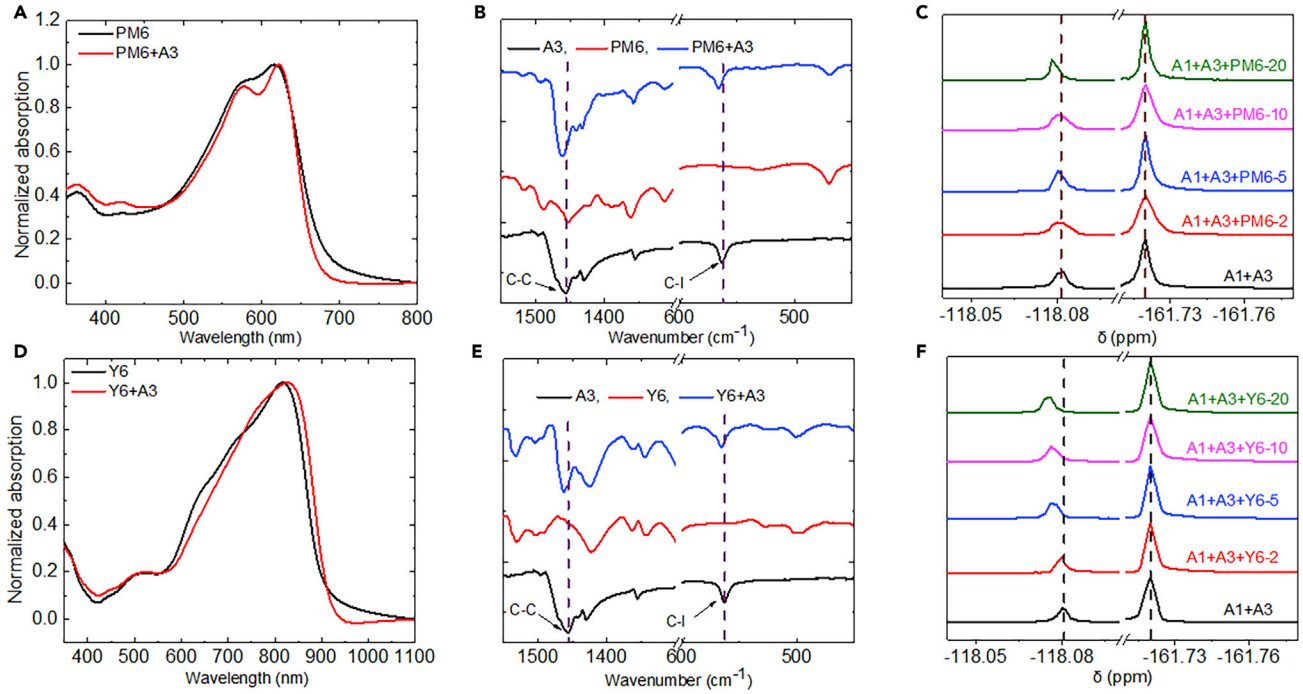

Figure 4. Spectroscopy of A3-Induced Photoactive Materials

(A) Absorption spectra of PM6 and PM6:A3 films.

(B) FTIR spectra of A3, PM6, and PM6:A3.

(C) ^{19}F NMR change of A3 (5 mg/mL) upon addition of PM6 (0–20 mg/mL). A1, hexafluorobenzene (5 mg/mL) was used as internal standard.

(D) Absorption spectra of Y6 and Y6:A3 films.

(E) FTIR spectra of A3, Y6, and Y6:A3.

(F) ^{19}F NMR change of A3 (5 mg/mL) upon addition of Y6 (0–20 mg/mL). A1, hexafluorobenzene (5 mg/mL) was used as internal standard.

the TA-treated PM6:Y6:A3 blend film (Figure S5) disappear, again verifying the statement above. The evaporation process under TA was recorded. As shown in Figure S6, A3 with the optimum device amount wholly disappeared within 1 min. On increasing the amount of A3 up to 30 mg, the volatilization process can complete within 15 min. Based on these results, we believe that the non-covalent nature of the σ-hole interaction ensures that A3 is evaporable, even though weak interactions exist between A3 and the active layer

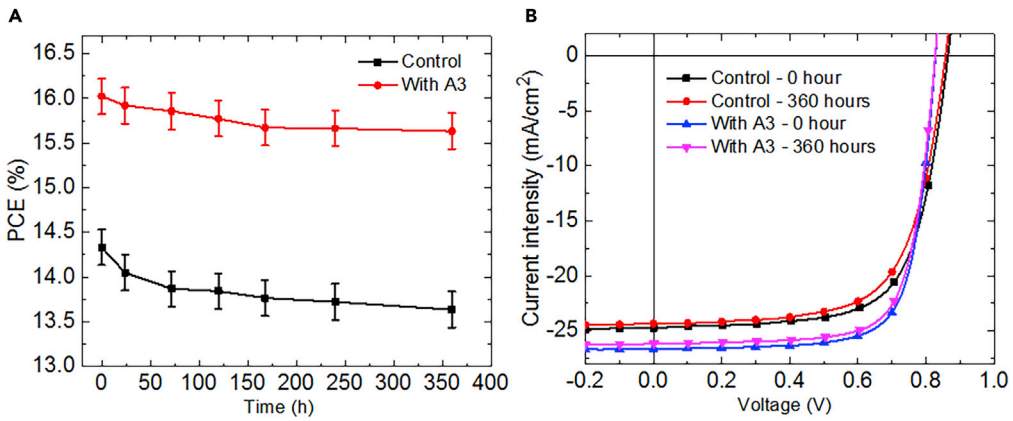

Figure 5. Long-term Stability Test of PM6: Y6-Based OSCs (without Encapsulation) Treated with or without A3

(A) PCE changes of devices with or without A3 as a function of storage time; see also Table S5 and Table S6.

(B) J–V curves for fresh and aged devices with or without A3.

materials. To study the effect of A3 on the long-term storage stability of OSCs based on PM6 and Y6, we stored the devices processed with or without A3 in a N_2-filled glovebox. Although there was no encapsulation, the A3-treated device still maintained 97.5% of its initial average efficiency after 360-h storage (Table S5 and Figure 5A), higher than the value of its control counterpart (95.1% of its average PCE, presented in Table S6 and Figure 5B). Thus, the volatility of A3 additive is appropriate in the high-efficiency PM6:Y6 system.

DISCUSSION

In summary, a novel σ-hole-containing volatile solid additive A3 was developed for high-performance non-fullerene OSCs. Through the synergetic halogen bonding interaction between A3 and photoactive materials, thermodynamically preferred face-on orientation with orderly denser molecular stacking was realized in the BHJ blend films, contributing to less recombination and better charge transport properties. Assisted by A3 additive, a great PCE of 16.5% (certified as 15.9%) with excellent stability in devices was achieved, significantly higher than the reported efficiency using traditional CN additive (certified as 14.9%). Notably, the utilization of A3 can maintain a decent efficiency over 16.0% even within a wide concentration range of A3 additive from 10 to 35 mg/mL in the precursor solution. The intermolecular interaction via halogen bonding was demonstrated to be a feasible method for improving the performance of non-fullerene OSCs. The success of A3 additive treatment paves an avenue for designing volatile solid additives for the large-scale production of high-performance OSCs.

Limitations of the Study

There are many other σ-hole-containing small molecules; here we studied one successful example. A lot of otherσ-hole-containing additives can be explored.

METHODS

All methods can be found in the accompanying Transparent Methods supplemental file.

SUPPLEMENTAL INFORMATION

Supplemental Information can be found online at https://doi.org/10.1016/j.isci.2020.100965.

ACKNOWLEDGMENTS

This work was financially supported by research grants from the National Youth Thousand Program Project (R52A199Z11), National Natural Science Foundation of China (61504015 and 21801238), CAS Pioneer Hundred Talents Program B (Y92A010Q10), National Special Funds for Repairing and Purchasing Scientific Institutions (Y72Z090Q10), the Natural Science Foundation of Chongqing (cstc2017jcyjA0752, cstc2018jcyjAX0556, cstc2017jcy-jAX0384, and cstc2018jszx-cyzdX0137), the "artificial intelligence" key project of Chongqing (No. cstc2017rgzn-zdyfX0030), the Key Laboratory of Low-grade Energy Utilization Technologies and Systems (LLEUTS-2017004, LLEUTS-2019001), the Venture & Innovation Support Program for Chongqing Overseas Returnees (cx2017034, cx2019028), Chongqing Key Laboratory for Advanced Materials & Technologies of Clean Energies (Grant No. JJNY201909), and the Youth Innovation Fund (Y82A260Q10).

AUTHOR CONTRIBUTIONS

J.F. fabricated the devices and performed the morphology characterization and analysis. K.Y., S.J., J.L., L.L., H.C., D.H., and Q.Y. performed the TPV, TPC, FTIR, TGA experiments and DFT calculations, which were supervised by S.C., Z.K., T.D., K.S., S.L., and Z.X. K.S., S.L., J.F., and Z.X. conceived the study. J.F. wrote the manuscript. S.C., Z.X., and Y.L. revised the manuscript. All authors have contributed to the manuscript revision.

DECLARATION OF INTERESTS

The authors declare no competing interests.

Received: December 14, 2019
Revised: February 22, 2020
Accepted: March 3, 2020
Published: March 27, 2020

REFERENCES

Baran, D., Kirchartz, T., Wheeler, S., Dimitrov, S., Abdelsamie, M., Gorman, J., Ashraf, R.S., Holliday, S., Wadsworth, A., and Gasparini, N. (2016). Reduced voltage losses yield 10% efficient fullerene free organic solar cells with >1 V open circuit voltages. Energy Environ. Sci. *9*, 3783–3793.

Cavallo, G., Metrangolo, P., Milani, R., Pilati, T., Priimagi, A., Resnati, G., and Terraneo, G. (2016). The halogen bond. Chem. Rev. *116*, 2478–2601.

Cui, Y., Yao, H., Zhang, J., Zhang, T., Wang, Y., Hong, L., Xian, K., Xu, B., Zhang, S., and Peng, J. (2019). Over 16% efficiency organic photovoltaic cells enabled by a chlorinated acceptor with increased open-circuit voltages. Nat. Commun. *10*, 2515.

Erb, T., Zhokhavets, U., Gobsch, G., Raleva, S., Stühn, B., Schilinsky, P., Waldauf, C., and Brabec, C.J. (2005). Correlation between structural and optical properties of composite polymer/fullerene films for organic solar cells. Adv. Funct. Mater. *15*, 1193–1196.

Fei, Z., Eisner, F.D., Jiao, X., Azzouzi, M., Röhr, J.A., Han, Y., Shahid, M., Chesman, A.S.R., Easton, C.D., and Mcneill, C.R. (2018). An alkylated indacenodithieno[3,2-b] thiophene-based nonfullerene acceptor with high crystallinity exhibiting single junction solar cell efficiencies greater than 13% with low voltage losses. Adv. Mater. *30*, 1705209.

Hai, Y.G., Qian, J.S., Xiao, R.Z., Xiao, Q.Y., Xue, P., and Wei, J.J. (2012). Phosphorescent co-crystal assembled by 1,4-diiodotetrafluorobenzene with carbazole based on C–I···π halogen bonding. J. Mater. Chem. *22*, 5336–5343.

Hanson, G.R., Jensen, P., McMurtrie, J., Rintoul, L., and Micallef, A.S. (2009). Halogen bonding between an isoindoline nitroxide and 1,4-diiodotetrafluorobenzene: new tools and tectons for self-assembling organic spin systems. Chem. Eur. J. *15*, 4156–4164.

Hong, L., Yao, H., Wu, Z., Cui, Y., Zhang, T., Xu, Y., Yu, R., Liao, Q., Gao, B., and Xian, K. (2019). Eco-compatible solvent-processed organic photovoltaic cells with over 16% efficiency. Adv. Mater. *31*, 1903441.

Hoven, C.V., Dang, X.D., Coffin, R.C., Peet, J., Nguyen, T.Q., and Bazan, G.C. (2010). Improved performance of polymer bulk heterojunction solar cells through the reduction of phase separation via solvent additives. Adv. Mater. *22*, E63–E66.

Huang, W., Cheng, P., Yang, Y., Li, G., and Yang, Y. (2018). High-performance organic bulk-heterojunction solar cells based on multiple-donor or multiple-acceptor components. Adv. Mater. *30*, 1705706.

Hummelen, J.C., Knight, B.W., LePeq, F., Wudl, F., Yao, J., and Wilkins, C.L. (1995). Preparation and characterization of fulleroid and methanofullerene derivatives. J. Org. Chem. *60*, 532–538.

Jiang, K., Wei, Q., Lai, J.Y.L., Peng, Z., Kim, H.K., Yuan, J., Ye, L., Ade, H., Zou, Y., and Yan, H. (2019). Alkyl chain tuning of small molecule acceptors for efficient organic solar cells. Joule *3*, 3020–3033.

Kim, Y., Choulis, S.A., Nelson, J., Bradley, D.D.C., Cook, S., and Durrant, J.R. (2005). Device annealing effect in organic solar cells with blends of regioregular poly(3-hexylthiophene) and soluble fullerene. Appl. Phys. Lett. *86*, 063502.

Kolář, M.H., and Hobza, P. (2016). Computer modeling of halogen bonds and other σ-hole interactions. Chem. Rev. *116*, 5155–5187.

Lee, J.K., Ma, W.L., Brabec, C.J., Yuen, J., Moon, J.S., Kim, J.Y., Lee, K., Bazan, G.C., and Heeger, A.J. (2008). Processing additives for improved efficiency from bulk heterojunction solar cells. J. Am. Chem. Soc. *130*, 3619–3623.

Li, G., Shrotriya, V., Huang, J., Yao, Y., Moriarty, T., Emery, K., and Yang, Y. (2005). High-efficiency solution processable polymer photovoltaic cells by self-organization of polymer blends. Nat. Mater. *4*, 864–868.

Li, G., Yao, Y., Yang, H., Shrotriya, V., Yang, G., and Yang, Y. (2010). "Solvent annealing" effect in polymer solar cells based on poly(3-hexylthiophene) and methanofullerenes. Adv. Funct. Mater. *17*, 1636–1644.

Li, S., Ye, L., Zhao, W., Yan, H., Yang, B., Liu, D., Li, W., Ade, H., and Hou, J. (2018). A wide band gap polymer with a deep highest occupied molecular orbital level enables 14.2% efficiency in polymer solar cells. J. Am. Chem. Soc. *140*, 7159–7167.

Liang, R.Z., Babics, M., Savikhin, V., Zhang, W., Le Corre, V.M., Lopatin, S., Kan, Z., Firdaus, Y., Liu, S., and McCulloch, I. (2018). Carrier transport and recombination in efficient "all-small-molecule" solar cells with the nonfullerene acceptor IDTBR. Adv. Energy Mater. *8*, 1800264.

Lim, J.Y.C., and Beer, P.D. (2018). Sigma-hole interactions in anion recognition. Chem *4*, 731–783.

Lin, Y., Wang, J., Zhang, Z.G., Bai, H., Li, Y., Zhu, D., and Zhan, X. (2015). An electron acceptor challenging fullerenes for efficient polymer solar cells. Adv. Mater. *27*, 1170–1174.

Liu, C.Z., Koppireddi, S., Wang, H., Zhang, D.W., and Li, Z.T. (2019a). Halogen bonding directed supramolecular quadruple and double helices from hydrogen-bonded arylamide foldamers. Angew. Chem. Int. Ed. *58*, 226–230.

Liu, C.Z., Koppireddi, S., Wang, H., Zhang, D.W., and Li, Z.T. (2019b). Halogen bonding directed supramolecular quadruple and double helices from hydrogen-bonded arylamide foldamers. Angew. Chem. Int. Ed. *131*, 232–236.

Ma, W.L., Yang, C.Y., Gong, X., Lee, K.H., and Heeger, A.J. (2010). Thermally stable, efficient polymer solar cells with nanoscale control of the interpenetrating network morphology. Adv. Funct. Mater. *15*, 1617–1622.

Machui, F., Maisch, P., Burgués-Ceballos, I., Langner, S., Krantz, J., Ameri, T., and Brabec, C.J. (2015). Classification of additives for organic photovoltaic devices. ChemPhysChem *16*, 1275–1280.

Manley, E.F., Strzalka, J., Fauvell, T.J., Jackson, N.E., Leonardi, M.J., Eastham, N.D., Marks, T.J., and Chen, L.X. (2017). In situ GIWAXS analysis of solvent and additive effects on PTB7 thin film microstructure evolution during spin coating. Adv. Mater. *29*, 1703933.

Más-Montoya, M., and Janssen, R.A.J. (2017). The effect of H- and J-aggregation on the photophysical and photovoltaic properties of small thiophene-pyridine-DPP molecules for bulk-heterojunction solar cells. Adv. Funct. Mater. *27*, 1605779.

Mcdowell, C., Abdelsamie, M., Toney, M.F., and Bazan, G.C. (2018). Solvent additives: key morphology-directing agents for solution-processed organic solar cells. Adv. Mater. *30*, 1707114.

Pan, F., Sun, C., Li, Y., Tang, D., Zou, Y., Li, X., Bai, S., Wei, X., Lv, M., and Chen, X. (2019). Solution-processable n-doped graphene-containing cathode interfacial materials for high performance organic solar cells. Energy Environ. Sci. *12*, 3400–3411.

Peet, J., Soci, C., Coffin, R.C., Nguyen, T.Q., Mikhailovsky, A., Moses, D., and Bazan, G.C. (2006). Method for increasing the photoconductive response in conjugated polymer/fullerene composites. Appl. Phys. Lett. *89*, 252105.

Peet, J., Kim, J.Y., Coates, N.E., Ma, W.L., Moses, D., Heeger, A.J., and Bazan, G.C. (2007). Efficiency enhancement in low-bandgap polymer solar cells by processing with alkane dithiols. Nat. Mater. *6*, 497–500.

Rogers, J.T., Schmidt, K., Toney, M.F., Kramer, E.J., and Bazan, G.C. (2011). Structural order in bulk heterojunction films prepared with solvent additives. Adv. Mater. *23*, 2284–2288.

Sarwar, M.G., Dragisic, B., Salsberg, L.J., Gouliaras, C., and Taylor, M.S. (2010). Thermodynamics of halogen bonding in solution: substituent, structural, and solvent effects. J. Am. Chem. Soc. *132*, 1646–1653.

Schulz, G.L., and Ludwigs, S. (2017). Controlled crystallization of conjugated polymer films from solution and solvent vapor for polymer electronics. Adv. Funct. Mater. *27*, 1603083.

Shockley, W., and Jr, W.T.R. (1952). Statistics of the recombinations of holes and electrons. Phys. Rev. *87*, 835–842.

Sun, K., Xiao, Z., Hanssen, E., Klein, M.F.G., Dam, H.H., Pfaff, M., Gerthsen, D., Wong, W.W.H., and Jones, D.J. (2014). The role of solvent vapor annealing in highly efficient air-processed small molecule solar cells. J. Mater. Chem. A *2*, 9048–9054.

Sun, K., Xiao, Z.Y., Lu, S.R., Zajaczkowski, W., Pisula, W., Hanssen, E., White, J.M., Williamson, R.M., Subbiah, J., Ouyang, J.Y., et al. (2015). A molecular nematic liquid crystalline material for high-performance organic photovoltaics. Nat. Commun. *6*, 6013.

Tan, W.Y., Wang, R., Li, M., Liu, G., Chen, P., Li, X.C., Lu, S.M., Zhu, H.L., Peng, Q.M., and Zhu, X.H. (2015). Lending triarylphosphine oxide to phenanthroline: a facile approach to high-performance organic small-molecule cathode interfacial material for organic photovoltaics utilizing air-stable cathodes. Adv. Funct. Mater. *24*, 6540–6547.

Tournebize, A., Rivaton, A., Peisert, H., and Chassé, T. (2015). The crucial role of confined residual additives on the photostability of P3HT:PCBM active layers. J. Phys. Chem. C *119*, 9142–9148.

Villers, B.J.T.D., O'Hara, K.A., Ostrowski, D.P., Biddle, P.H., Shaheen, S.E., Chabinyc, M.L., Olson, D.C., and Kopidakis, N. (2016). Removal of residual diiodooctane improves photostability of high-performance organic solar cell polymers. Chem. Mater. *28*, 876–884.

Wang, H., and Jin, W.J. (2017). Cocrystal assembled by 1, 4-diiodotetrafluorobenzene and phenothiazine based on C—I···π/N/S halogen bond and other assisting interactions. Acta Crystallogr. B Struct. Sci. Cryst. Eng. Mater. *73*, 210–216.

Wienk, M.M., Kroon, J.M., Verhees, W.J., Knol, J., Hummelen, J.C., van Hal, P.A., and Janssen, R.A. (2003). Efficient methano [70] fullerene/MDMO-PPV bulk heterojunction photovoltaic cells. Angew. Chem. Int. Ed. *42*, 3371–3375.

Yan, T., Song, W., Huang, J., Peng, R., Huang, L., and Ge, Z. (2019). 16.67% rigid and 14.06% flexible organic solar cells enabled by ternary heterojunction strategy. Adv. Mater. *31*, 1902210.

Yang, Y.M., Chen, W., Dou, L., Chang, W.-H., Duan, H.-S., Bob, B., Li, G., and Yang, Y. (2015). High-performance multiple-donor bulk heterojunction solar cells. Nat. Photon. *9*, 190.

Yu, R., Yao, H., Hong, L., Qin, Y., Zhu, J., Cui, Y., Li, S., and Hou, J. (2018). Design and application of volatilizable solid additives in non-fullerene organic solar cells. Nat. Commun. *9*, 4645.

Yu, Z.-P., Liu, Z.-X., Chen, F.-X., Qin, R., Lau, T.-K., Yin, J.-L., Kong, X., Lu, X., Shi, M., and Li, C.-Z. (2019). Simple non-fused electron acceptors for efficient and stable organic solar cells. Nat. Commun. *10*, 2152.

Yuan, J., Zhang, Y., Zhou, L., Zhang, G., Yip, H.-L., Lau, T.-K., Lu, X., Zhu, C., Peng, H., and Johnson, P.A. (2019). Single-junction organic solar cell with over 15% efficiency using fused-ring acceptor with electron-deficient core. Joule *3*, 1140–1151.

Zhang, S., Qin, Y., Zhu, J., and Hou, J. (2018a). Over 14% efficiency in polymer solar cells enabled by a chlorinated polymer donor. Adv. Mater. *30*, 1800868.

Zhang, T., Zhao, X., Yang, D., Tian, Y., and Yang, X. (2018b). Ternary organic solar cells with> 11% efficiency incorporating thick photoactive layer and nonfullerene small molecule acceptor. Adv. Energy Mater. *8*, 1701691.

Zhao, W., Li, S., Yao, H., Zhang, S., Zhang, Y., Yang, B., and Hou, J. (2017). Molecular optimization enables over 13% efficiency in organic solar cells. J. Am. Chem. Soc. *139*, 7148–7151.

iScience, Volume *23*

Supplemental Information

A "σ-Hole"-Containing Volatile Solid Additive Enabling 16.5% Efficiency Organic Solar Cells

Jiehao Fu, Shanshan Chen, Ke Yang, Sungwoo Jung, Jie Lv, Linkai Lan, Haiyan Chen, Dingqin Hu, Qianguang Yang, Tainan Duan, Zhipeng Kan, Changduk Yang, Kuan Sun, Shirong Lu, Zeyun Xiao, and Yongfang Li

Supplementary Figures

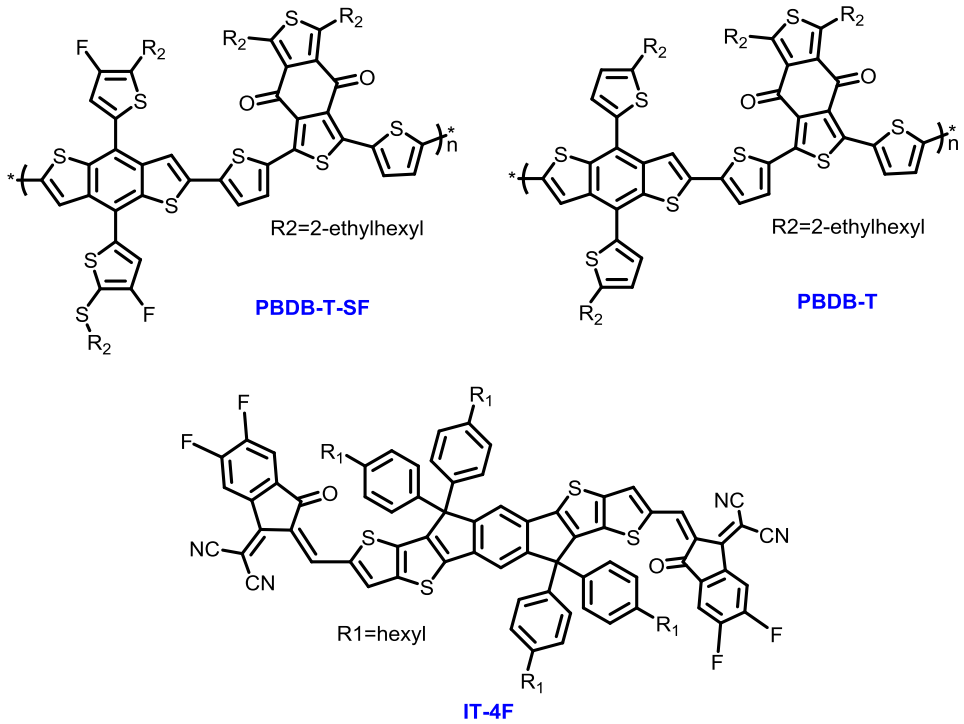

Supplementary Figure S1 Molecule structures of donors (PBDBT and PBDBT-SF) and acceptor (IT-4F) used in this work to demonstrate the versatility of A3. Related to Figure 1.

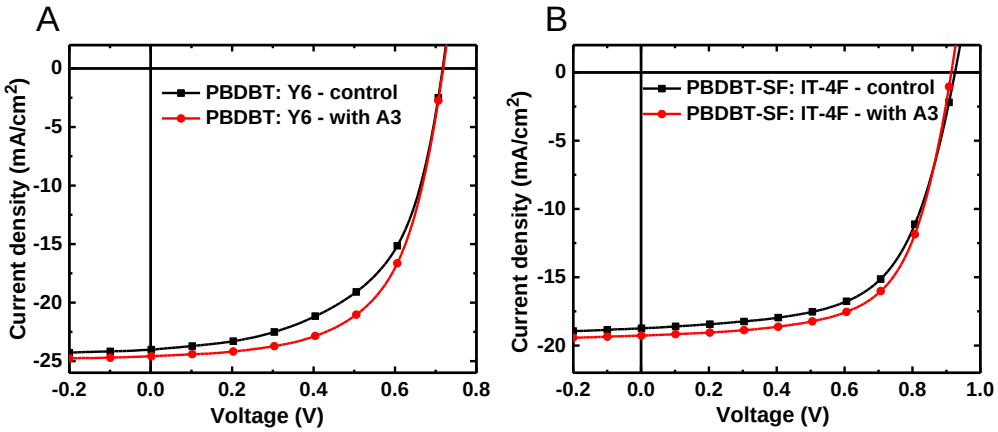

Supplementary Figure S2 J-V Curves of OSCs processed with or without A3 (10 mg/mL). (**A**) PBDBT: Y6-based devices, (**B**) PBDBT-SF: IT-4F-based devices. Related to Figure 1.

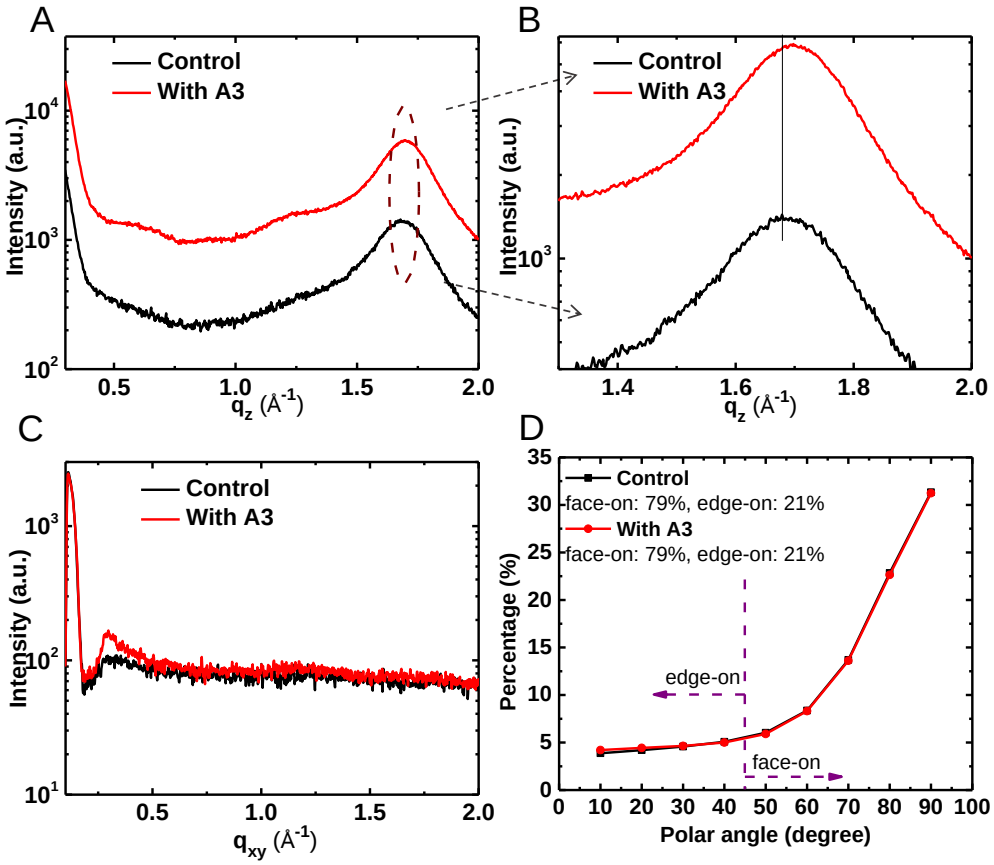

Supplementary Figure S3. Extracted 1D GIWAXS profiles along the OOP (**A**) and IP (**C**) directions. (**B**) Zoomed-in 1D GIWAXS profiles (OOP direction) in the range of 1.3-2 Å^{-1}. (**D**) The intensity azimuthal pole figure of (010) diffractions of the control and A3 treated films. Related to Figure 3C and 3F.

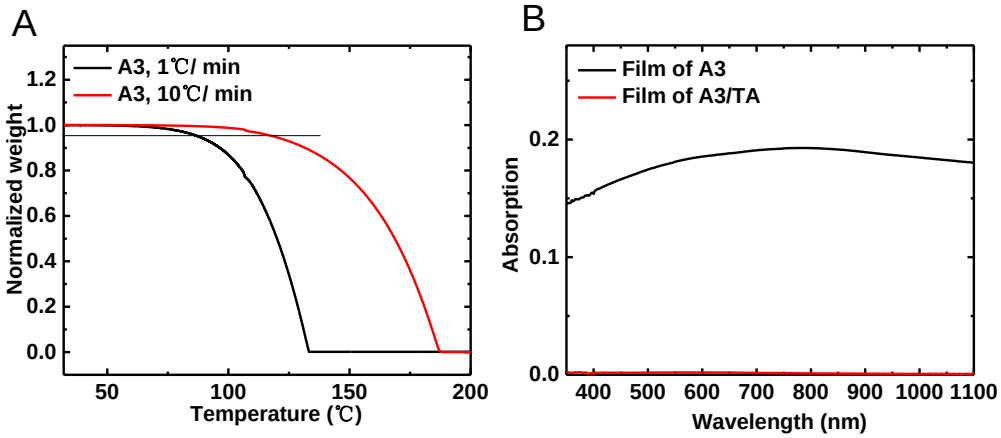

Supplementary Figure S4 (**A**) TGA of A3 at different scan rates. (**B**) Absorption spectra of coated films of A3 with or without TA process. Related to Figure 5.

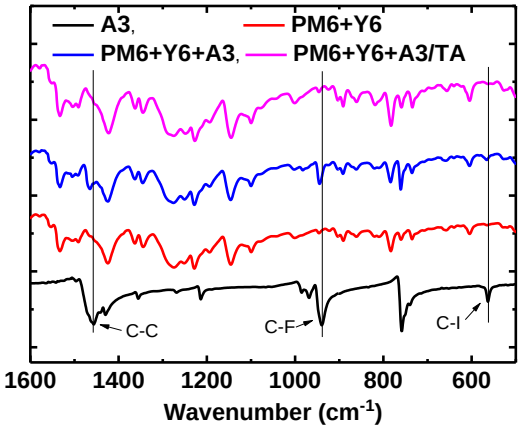

Supplementary Figure S5 FTIR spectra of A3, PM6:Y6, PM6:Y6:A3 and PM6:Y6:A3/TA. Related to Figure 5.

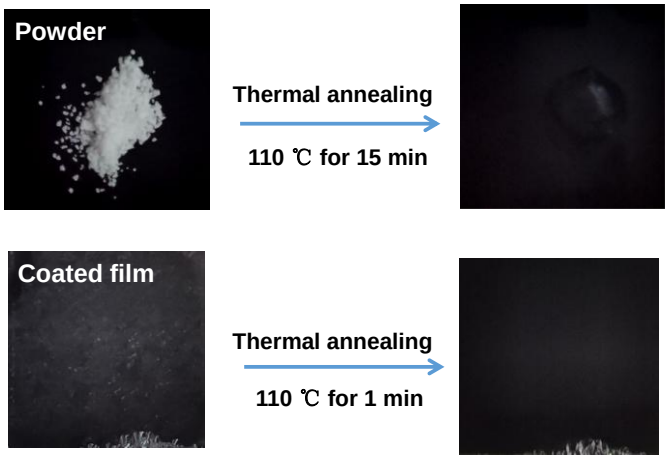

Supplementary Figure S6 Photos of A3 powders and the respective spin-coated film on Si substrates. Then the films were thermal annealed until A3 vanished. Related to Figure 5.

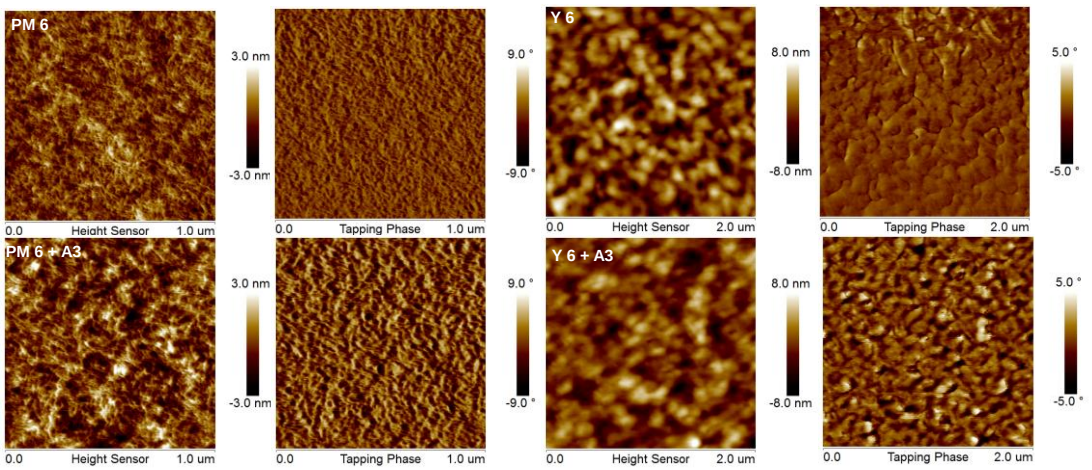

Supplementary Figure S7 PM6 film and Y6 film morphology changes upon A3 treatment. Related to Figure 4.

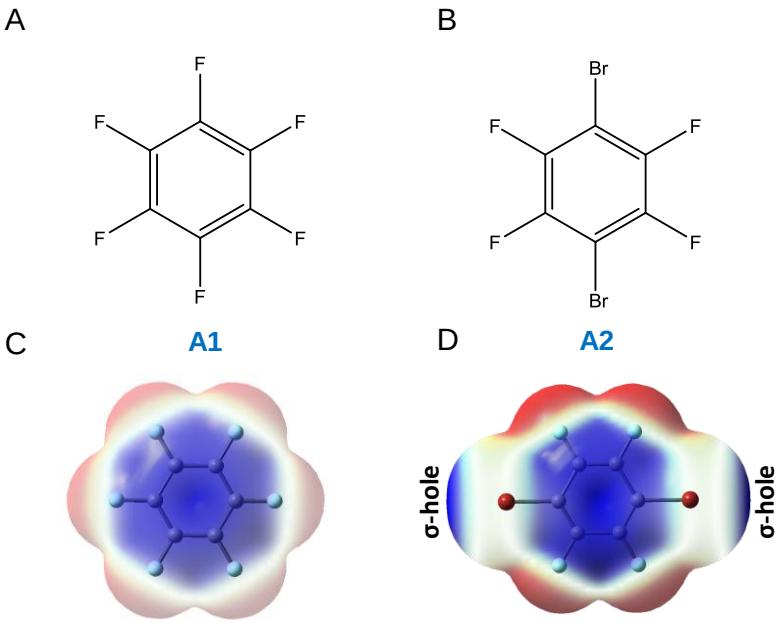

Supplementary Figure S8 Molecule structures and corresponding ESPs of A1 and A2. The ESPs were calculated from the DFT at the BLYP/6－31G level. Related to Figure 4.

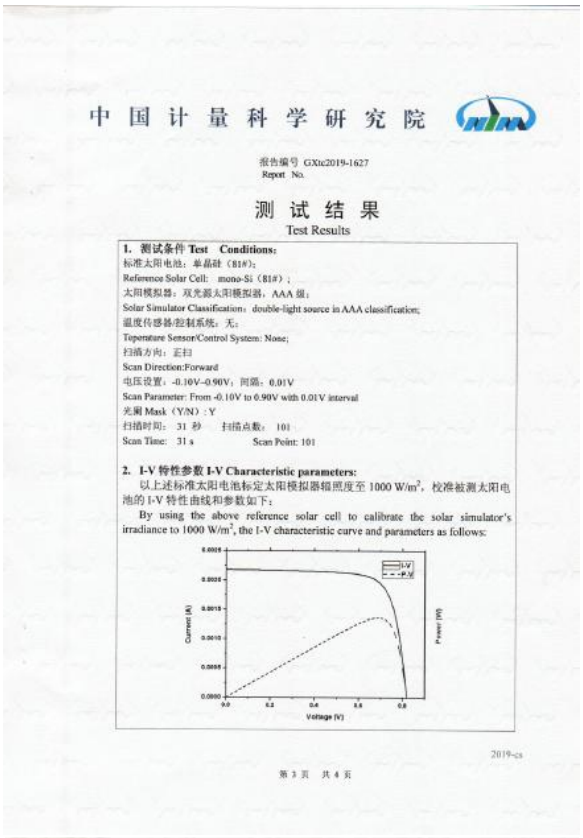

中 国 计 量 科 学 研 究 院

报告编号 GXtc2019-1627
Report No.

测 试 结 果
Test Results

1. 测试条件 Test Conditions:

标准太阳电池：单晶硅（81#）;
Reference Solar Cell: mono-Si（81#）;
太阳模拟器：双光源太阳模拟器，AAA 级;
Solar Simulator Classification: double-light source in AAA classification;
温度传感器/控制系统：无;
Tepentare Sensor/Control System: None;
扫描方向：正扫
Scan Direction:Forward
电压设置：-0.10V~0.90V；间隔：0.01V
Scan Parameter: From -0.10V to 0.90V with 0.01V interval
光阑 Mask（Y/N）：Y
扫描时间： 31 秒 扫描点数： 101
Scan Time: 31 s Scan Point: 101

2. I-V 特性参数 I-V Characteristic parameters:

以上述标准太阳电池标定太阳模拟器辐照度至 1000 W/m^2，校准被测太阳电池的 I-V 特性曲线和参数如下：

By using the above reference solar cell to calibrate the solar simulator's irradiance to 1000 W/m^2, the I-V characteristic curve and parameters as follows:

2019-cs

第 3 页 共 4 页

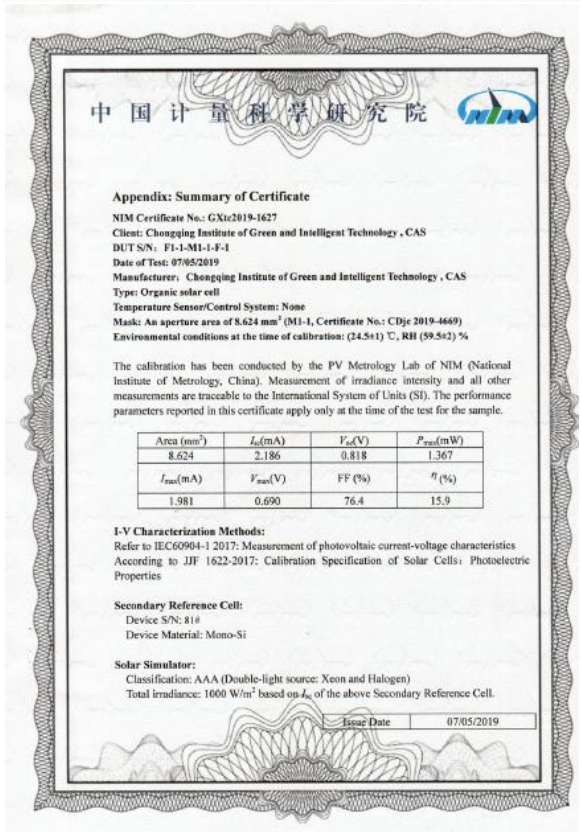

中 国 计 量 科 学 研 究 院

Appendix: Summary of Certificate

NIM Certificate No.: GXtc2019-1627
Client: Chongqing Institute of Green and Intelligent Technology , CAS
DUT S/N: F1-1-M1-1-F-1
Date of Test: 07/05/2019
Manufacturer: Chongqing Institute of Green and Intelligent Technology , CAS
Type: Organic solar cell
Temperature Sensor/Control System: None
Mask: An aperture area of 8.624 mm^2 (M1-1, Certificate No.: CDje 2019-4669)
Environmental conditions at the time of calibration: (24.5±1) ℃, RH (59.5±2) %

The calibration has been conducted by the PV Metrology Lab of NIM (National Institute of Metrology, China). Measurement of irradiance intensity and all other measurements are traceable to the International System of Units (SI). The performance parameters reported in this certificate apply only at the time of the test for the sample.

Area (mm^2)	I_{sc}(mA)	V_{oc}(V)	P_{max}(mW)
8.624	2.186	0.818	1.367
I_{max}(mA)	V_{max}(V)	FF (%)	η (%)
1.981	0.690	76.4	15.9

I-V Characterization Methods:
Refer to IEC60904-1 2017: Measurement of photovoltaic current-voltage characteristics
According to JJF 1622-2017: Calibration Specification of Solar Cells: Photoelectric Properties

Secondary Reference Cell:
Device S/N: 81#
Device Material: Mono-Si

Solar Simulator:
Classification: AAA (Double-light source: Xeon and Halogen)
Total irradiance: 1000 W/m^2 based on I_{sc} of the above Secondary Reference Cell.

Issue Date	07/05/2019

Supplementary Figure S9 The copy images of PCE certificate of PM6:Y6-based OSC processed with A3 from National Institute of Metrology, China (NIM). Related to Figure 1.

Supplemental Tables

Table S1 Photovoltaic performances of PM6:Y6-based OSCs with different concentration of A3 additive. All of cells performed without any treatment. Related to Table 1.

Concentration of additive	V_{OC} (V)	J_{SC} (mA cm^{-2})	FF (%)	PCE[a]. (%)
0	0.86	25.29	68.40	14.8 (14.5±0.2)
5 mg/ml	0.86	24.84	69.54	14.8 (14.6±0.1)
10 mg/ml	0.84	25.92	69.15	15.0 (14.8±0.1)
15 mg/ml	0.84	25.36	71.63	15.2 (14.9±0.2)
20 mg/ml	0.83	25.08	70.29	14.6 (14.3±0.2)
35 mg/ml	0.78	22.58	62.71	11.0 (10.6±0.2)
50 mg/ml	0.29	7.56	18.52	0.4 (0.3±0.1)

[a]The average PCEs with standard deviation from the mean are calculated from 20+ devices and shown in the parenthesis.

Table S2 The effect of A3 on the device performance of different non-fullerene OSCs. Related to Figure 1.

Active layer	Condition	V_{OC} (V)	J_{SC} (mA cm^{-2})	FF (%)	PCE[a]. (%)
PBDB-T: Y6	Control	0.72	24.02	56.66	9.8 (9.6±0.1)
	With A3	0.72	24.59	61.24	10.8 (10.6±0.1)
PBDB-T-SF: IT4F	Control	0.92	18.74	62.19	10.7 (10.5±0.1)
	With A3	0.91	19.28	64.66	11.3 (11.1±0.1)

[a]The average PCEs with standard deviation from the mean are calculated from 15 devices and shown in the parenthesis.

Table S3 Charge mobilities from SCLC method for PM6:Y6-based films with or without A3 additive. Related to Figure 2.

Active layer	μ_h (cm^2 V^{-1} s^{-1})	μ_e (cm^2 V^{-1} s^{-1})	μ_h/μ_e
Control	3.08×10^{-4}	1.32×10^{-4}	2.33
A3	4.84×10^{-4}	3.96×10^{-4}	1.22

Table S4 Detailed data for GIWAXS measurements. Related to Figure 3C and 3F.

Q_{xy}	Location ($Å^{-1}$)	d-spacing (Å)	FWHM ($Å^{-1}$)	CCL (Å)
(100)[a]	0.288	21.796	0.065	87.321
(100)[b]	0.287	21.875	0.062	91.075
Q_z	Location ($Å^{-1}$)	d-spacing (Å)	FWHM ($Å^{-1}$)	CCL (Å)
(010)[a]	1.690	3.717	0.214	26.750
(010)[b]	1.700	3.696	0.207	27.630

[a]The control film, [b]modified film by A3 additive.

Table S5 Performance parameters of A3-treated OSCs without encapsulation stored in a N_2-filled glovebox. Related to Figure 5.

Storage time (h)	V_{OC} (V)	J_{SC} (mA cm^{-2})	FF (%)	PCE[a]. (%)
0	0.82	26.62	75.02	16.4 (16.0±0.2)
24	0.82	26.71	74.33	16.2 (15.9±0.2)
72	0.82	26.11	75.21	16.1 (15.8±0.2)
120	0.82	26.11	75.02	16.1 (15.7±0.2)
168	0.82	26.35	74.13	16.0 (15.7±0.2)
240	0.82	26.19	74.53	16.0 (15.7±0.2)
360	0.82	26.15	74.63	15.9 (15.6±0.2)

[a]The active layer is the combination of PM6 and Y6. And the average PCEs with standard deviation from the mean are calculated from 12+ devices and shown in the parenthesis.

Table S6 Performance parameters of control samples without encapsulation stored in a N_2-filled glovebox. Related to Figure 5.

Storage time (h)	V_{OC} (V)	J_{SC} (mA cm^{-2})	FF (%)	PCE[a]. (%)
0	0.86	24.73	68.97	14.6 (14.3±0.2)
24	0.86	24.65	67.64	14.3 (14.0±0.2)
72	0.86	24.56	67.01	14.2 (13.9±0.2)
120	0.86	24.66	66.62	14.1 (13.8±0.2)
168	0.85	24.48	67.52	14.1 (13.8±0.2)
240	0.85	24.52	67.17	14.0 (13.7±0.2)
360	0.85	24.34	67.25	13.9 (13.6±0.2)

[a]The active layer is the combination of PM6 and Y6. And the average PCEs with standard deviation from the mean are calculated from 12+ devices and shown in the parenthesis.

Table S7 Photovoltaic performances of PM6:Y6-based OSCs with different additives. Related to Figure 4.

Additive	V_{OC} [V]	J_{SC} [mA cm^{-2}]	FF [%]	PCE[a]. [%]
W/O (Control)	0.86	25.29	68.40	14.8 (14.5±0.2)
W/O-TA	0.84	25.88	67.79	14.7 (14.5±0.1)
A1	0.84	26.13	67.71	14.9 (14.5±0.3)
A2	0.83	25.92	74.71	16.1 (15.8±0.1)
A3	0.82	26.50	76.05	16.5 (16.1±0.2)

[a]The average PCEs with standard deviation from the mean are calculated from 20 devices and shown in the parenthesis.

Table S8 PCEs and the corresponding additives of recent high performance OSCs based on non-fullerene acceptors. Related to Figure 1.

Active materials	Additive	Optimum volume	Active area (cm^2)	PCE (%)	Reference
PBDBT-2Cl: IT-4F	SA-1, solid	17.3 wt% of acceptor (1.9 mg/ml)	0.04	14.2	(Yu et al., 2018)
PBDBT-2Cl: IT-4F	DIO, solvent	1% (v/v)	0.04	14.4	(Zhang et al., 2018)
PM6: Y6	CN, solvent	0.5% (v/v)	0.04	15.7	(Yuan et al., 2019)
PM6: BTP-4F-12	DIO, solvent	0.5% (v/v)	0.037	16.4	(Hong et al., 2019)
S1: Y6	CN, solvent	0.5% (v/v)	0.059	16.4	(Sun et al., 2019)
PM6: BDP-4Cl	CN, solvent	0.5% (v/v)	0.09	16.5	(Cui et al., 2019)
PM6: Y6 (interfacial engineering)	CN, solvent	0.5% (v/v)	0.046	16.52	(Pan et al., 2019)
PM6:N3 (PM6:N3:PC71BM)	CN, solvent	0.05%	0.059	15.98 (16.74)	(Jiang et al., 2019)
PM6: Y6	A3, solid	229 wt% of acceptor (20 mg/ml)	0.11	16.5	This work

Transparent Methods

Materials

All materials are provided by commercial suppliers: ITO (YouXuan Tech.), PEDOT:PSS (Clevios P VP AI. 4083 (Heraeus)), PM6 (Solarmer Energy Inc.), Y6 (Derthon Ltd.), 1,4-Diiodotetrafluorobenzene (Fluorochem Ltd.), Phen-NaDPO (One Material Ltd.), Chloroform (J&K Scientific Ltd.), Isopropyl alcohol (J&K Scientific Ltd.) and Ag (ZNXC Ltd.). And all reagents and solvents are used directly without further purification.

Device fabrication and testing

The OSCs were fabricated with a conventional structure of ITO/PEDOT: PSS/active layer/Phen-NaDPO/Ag, where PEDOT: PSS and Phen-NaDPO are utilized as hole transport layer (HTL) and electron transport layer (ETL), respectively. At first, the ITO-coated glass substrates were cleaned sequentially with detergent, de-ionized water, acetone, and isopropyl alcohol (IPA) for 15 min under sonication. Then they were dried in nitrogen flow and treated with UV ozone for 15 min. After that, about 50 uL PEDOT:PSS was dripped on ITO substrates and spin-coated at 6000 rpm for 20 s, followed by thermal annealing on a hot plate at 120 ℃ for 20 min to remove the water in HTLs. Then, the substrates were transferred into a glovebox filled with nitrogen (O_2 < 10 ppm; H_2O < 10 ppm). For PM6:Y6 system, the total concentration of donor and acceptor (D:A=1:1.2, weight ratio) is 16 mg/mL. Firstly, chloroform solution with 20 mg/mL A3 additive was prepared. Then, the A3 chloroform solution is added to the solid PM6:Y6 blend according to their total weight. After stirring for 2 hour in glovebox at room temperature, the mixture of donor, acceptor and additive forms a homogeneous solution. Likewise, a precursor solution was prepared by mixing 5.2 mg PBDB-T, 7.8 mg Y6, and 10 mg A3 in 1 mL chloroform (for PBDB-T:Y6 system), or 4 mg PBDB-T-SF, 4 mg IT-4F, and 5 mg A3 in 1 mL chlorobenzenes (for PBDB-T-SF:IT-4F system). The mixed solution was spin-coated at 3000, 2000 and 1200 rpm for PM6:Y6, PBDB-T:Y6 and PBDB-T-SF:IT-4F systems, respectively, then TA for 10 min at 110 ℃ was employed to remove the

residue of A3 in active layer. The next stage is to coat ETL on active layer, about 40 uL Phen-NaDPO solution (0.5 mg/ml in IPA) was spin-coated at 2000 rpm for 30s. Finally, these semi-finished cells were transferred into a thermal evaporation chamber with a base pressure of approximately 2×10^{-4} Pa, where 100 nm Ag were deposited through a shadow mask with the active area of 11 mm^2. The current density–voltage (*J–V*) curves of OSCs were tested in air atmosphere by a Keithley 2400 source meter and an AAA grade solar simulator (Sirius-SS150A-D, Zolix Ltd.) along with AM 1.5 G spectra whose intensity was corrected by a certified standard silicon solar cell (Certificate No.: GXtc2017-1280, NIM) at 1000 W/m^2. The J-V curves are measured in the forward direction from 0.2 to 1.2 V. We also tested the efficiency of A3-based device using a metal mask with area of 8.624 mm^2 (Certificate No.: CDjc2019-4669, NIM) in the National Institute of Metrology (NIM), China, where we got a certified PCE of 15.9 % (Certificate No.: GXtc2019-1627, NIM) with a *Voc* of 0.818 V, an *Isc* of 2.186 mA and a FF of 0.764. The external quantum efficiency (EQE) was measured by a certified incident photon to electron conversion (IPCE) equipment (QE-R) from Enli Technology Co., Ltd.

Theoretically simulated ESP

The theoretically simulated electrostatic potential distribution (ESP) of A1, A2 and A3 are calculated from the density functional theory (DFT) at the BLYP/6–31G level. The colors changing from red to blue indicate the increasing ESP from negative to positive. To highlight the electrostatic potential positive and negative part, the electrostatic potential neutral parts of these additive molecules are processed with "transparent treatment", thus showing white color.

TPV&TPC

Transient photocurrent (TPC) and photovoltage (TPV) measurements: TPC were testing under the short-circuit condition to explore the time-dependent extraction of photogenerated charge carriers. The 10 ns light plus laser were selected to the light source for steady the photogenerated current density. The devices are otherwise kept in the dark between pulses in order to avoid any influence of pulse frequency on the current responses. TPV was testing under the open-circuit condition to explore the

photovoltage decay. The subsequent voltage decay is then recorded by the digital storage oscilloscope to directly monitor non-geminate charge carrier recombination. The intensity of light is 230 μW/cm^2 and the wavelength of light is 520 nm. The light pulse is 10 ns. The normalized curves are easier to compare the carrier lifetime and the slow decline one is the one with a long lifetime. The photovoltage decay kinetics of all devices follow a mono-exponential decay: $\delta V = A\exp(-t/\tau)$ where t is the time, and τ is the charge carrier lifetime, the fitting carrier lifetime value would not be affected by the A value. Thus the TPV curves are normalized.

SCLC mobility measurements

Electron-only devices with the structure of ITO/ZnO/DPO/active layer/DPO/Al and hole-only devices with the structure of ITO/MoO_3/active layer/ MoO_3/Ag are used to conduct SCLC measurements. The mobilities were determined by fitting the dark-field current density voltage curves using the Mott-Gurney relationship, which is described in the following equation,

$$\mathrm{J(V)} = \frac{9}{8}\varepsilon_0\varepsilon_r\mu_0\frac{V^2}{L^3}$$

where J is the current density, ε_0 is the permittivity of free space, ε_r is the relative permittivity of the material, μ_0 is the zero-field mobility, V is the effective voltage and L is the thickness of the active layer. From the plot of $J^{1/2}$ versus V, the hole and electron mobilities can be deduced.

AFM and GIWAXS

The atomic force microscopic (AFM) images were acquired using a Bruker Dimension EDGE in tapping mode. The GIWAXS data was obtained from the PLS-II 6A U-SAXS beamline of the Pohang Accelerator Laboratory in Korea. The active layer samples were deposited on the Si/PEDOT:PSS substrates followed device conditions. The X-rays coming from the in-vacuum undulator (IVU) were monochromated (wavelength λ=1.10994 Å) using a double crystal monochromated and focused both horizontally and vertically (450 (H) × 60 (V) μm2 in FWHM @ the sample position) using K-B type mirrors. The grazing incidence wide-angle X-ray

scattering sample stage was equipped with a 7-axis motorized stage for the fine alignment of the sample, and the incidence angles of the X-beam was set to be 0.11 °-0.13 °. The GIWAXS patterns were recorded with a 2D CCD detector (Rayonix SX165) and an X-ray irradiation time within 100s, dependent on the saturation level of the detector. Diffraction angles were calibrated using a sucrose standard (monoclinic, P21, a=10.8631 Å, b=8.7044 Å, c=7.7624 Å, and β=102.938°) and sample-to-detector distance was ~231 mm.

UV-vis, FTIR, and TGA

UV–Vis absorption spectra were determined by a Perkin Eimer Lambda 365 spectrophotometer. And the FTIR spectra were obtained by using an FTIR (UATR Two) spectrometer from Perkin Eimer Inc. Thermogravimetric analysis (TGA) was carried out on a Mettler Toledo TGA/DSC 1 thermogravimetric analyzer with a thermal balance under the protection of nitrogen.

Supplementary References

Yu, R., Yao, H., Hong, L., Qin, Y., Zhu, J., Cui, Y., Li, S. and Hou, J. (2018). Design and application of volatilizable solid additives in non-fullerene organic solar cells. *Nat. Commun*. 9, 4645.

Zhang, S., Qin, Y., Zhu, J. and Hou, J. (2018). Over 14% Efficiency in Polymer Solar Cells Enabled by a Chlorinated Polymer Donor. *Adv. Mater.* 30, 1800868.

Yuan, J., Zhang, Y., Zhou, L., Zhang, G., Yip, H.-L., Lau, T.-K., Lu, X., Zhu, C., Peng, H. and Johnson, P. A. (2019). Single-junction organic solar cell with over 15% efficiency using fused-ring acceptor with electron-deficient core. *Joule*. 3, 1140-1151.

Hong, L., Yao, H., Wu, Z., Cui, Y., Zhang, T., Xu, Y., Yu, R., Liao, Q., Gao, B. and Xian, K. (2019). Eco-Compatible Solvent-Processed Organic Photovoltaic Cells with Over 16% Efficiency. *Adv. Mater.* 31, 1903441.

Sun, H., Liu, T., Yu, J., Lau, T.-K., Zhang, G., Zhang, Y., Su, M., Tang, Y., Ma, R., Liu, B., *et al.* (2019). A monothiophene unit incorporating both fluoro and ester substitution enabling high-performance donor polymers for non-fullerene solar cells with 16.4% efficiency. *Energy Environ. Sci.* 12, 3328-3337.

Cui, Y., Yao, H., Zhang, J., Zhang, T., Wang, Y., Hong, L., Xian, K., Xu, B., Zhang, S. and Peng, J. (2019). Over 16% efficiency organic photovoltaic cells enabled by a chlorinated acceptor with increased open-circuit voltages. *Nature Commun*. 10, 2515.

Pan, F., Sun, C., Li, Y., Tang, D., Zou, Y., Li, X., Bai, S., Wei, X., Lv, M. and Chen, X. (2019). Solution-processable n-doped graphene-containing cathode interfacial materials for high performance organic solar cells. Energy Environ. Sci. 12, 3400-3411.

Jiang, K., Wei, Q., Lai, J. Y. L., Peng, Z., Kim, H. K., Yuan, J., Ye, L., Ade, H., Zou, Y. and Yan, H. (2019). Alkyl Chain Tuning of Small Molecule Acceptors for Efficient Organic Solar Cells. Joule. 3, 3020-3033.